Materials Today Bio 12 (2021) 100163

Contents lists available at ScienceDirect

Materials Today Bio

journal homepage: www.journals.elsevier.com/materials-today-bio

Potential of CO_2-laser processing of quartz for fast prototyping of microfluidic reactors and templates for 3D cell assembly over large scale

Elisabetta Perrone [a], Maura Cesaria [b,**], Alessandra Zizzari [a], Monica Bianco [a], Francesco Ferrara [a,c], Lillo Raia [d], Vita Guarino [a,b], Massimo Cuscunà [a], Marco Mazzeo [a,b], Giuseppe Gigli [a,b], Lorenzo Moroni [a,e], Valentina Arima [a,*]

[a] CNR NANOTEC - Institute of Nanotechnology, c/o Campus Ecotekne, Lecce, Italy
[b] University of Salento, Department of Mathematics and Physics "E. De Giorgi", Lecce, Italy
[c] STMicroelectronics S.r.l, Lecce, Italy
[d] STMicroelectronics S.r.l, Agrate Brianza, Monza Brianza, Italy
[e] Maastricht University, MERLN Institute for Technology-Inspired Regenerative Medicine, department of complex tissue regeneration, Maastricht, the Netherlands

ARTICLE INFO

Keywords:
CO_2-laser ablation
Microfluidics
Micro-reactors
3D cell assembly
Lab-on-a-Chip
Organ-on-a-Chip

ABSTRACT

Carbon dioxide (CO_2)-laser processing of glasses is a versatile maskless writing technique to engrave micro-structures with flexible control on shape and size.

In this study, we present the fabrication of hundreds of microns quartz micro-channels and micro-holes by pulsed CO_2-laser ablation with a focus on the great potential of the technique in microfluidics and biomedical applications. After discussing the impact of the laser processing parameters on the design process, we illustrate specific applications. First, we demonstrate the use of a serpentine microfluidic reactor prepared by combining CO_2-laser ablation and post-ablation wet etching to remove surface features stemming from laser-texturing that are undesirable for channel sealing. Then, cyclic olefin copolymer micro-pillars are fabricated using laser-processed micro-holes as molds with high detail replication. The hundreds of microns conical and square pyramidal shaped pillars are used as templates to drive 3D cell assembly. Human Umbilical Vein Endothelial Cells are found to assemble in a compact and wrapping way around the micro-pillars forming a tight junction network. These applications are interesting for both Lab-on-a-Chip and Organ-on-a-Chip devices.

1. Introduction

Patterning of microfluidic devices in glass supports/matrices is interesting to fabricate highly performant Lab-on-a-Chip (LoC) and Organ-on-a-Chip (OoC) devices for biological, medical and chemical applications [1–3] as well as to implement optofluidic elements [4]. Respect to other materials, such as polydimethylsiloxane (PDMS), Poly (methyl methacrylate) (PMMA) and SU-8 [5,6], glass is a convenient choice for manufacturing microfluidic chips due to its optical transparency, physical stability, chemical inertness, reusability, insulating properties, good dielectric properties, thermal stability, high resistance to mechanical stress, high solvent compatibility, biocompatibility and the possibility to process its surface for bonding to common micro-fabrication materials and for (bio)molecular functionalization [7,8].

Due to its isotropic nature, glass is typically micro-structured by wet (chemical) etching techniques, removing selectively the material under the same etching rate in all directions in the presence of specific masking layers [9–11]. Alternative conventional methods include deep reactive ion etching (DRIE) using chemically reactive plasma rather than solutions [12,13], glass molding [14–16], electrochemical discharge machining [17] and mechanical grinding [18]. Both wet and dry etching are conventionally applied in bulk micro-machining of glasses although may have some limitations in the control of the walls profile, the surface roughness, the etching rates, the integration density, the use of aggressive chemicals and the undercut that works against high aspect ratio structures. In general, although glass patterning techniques (such as photolithography, chemical/dry etching, thermal/anodic bonding, mechanical fabrication, photo-structuring, molding process [19,20]) allow to manufacture glass microfluidic platforms with geometrically

* Corresponding author.
** Corresponding author.
E-mail addresses: maura.cesaria@unisalento.it (M. Cesaria), valentina.arima@nanotec.cnr.it (V. Arima).

https://doi.org/10.1016/j.mtbio.2021.100163
Received 24 August 2021; Received in revised form 25 October 2021; Accepted 18 November 2021
Available online 22 November 2021

nonconventional and complex configurations, properly designed masks (mainly computer-designed and manufactured by lithography methods), hybrid technologies and multistep processing make the entire manufacturing process very complex, expensive and time-consuming [21].

Differently, microfluidic patterns as well as inlet/outlet ports can be generated directly on glass by laser micro-machining, consisting in the localized removal of materials by focused high-power pulsed laser beams strongly absorbed by the material to be processed [22–25]. Conveniently, laser ablation-based glass processing rules out long-processing time and the usage of projection custom-designed photomasks, expensive and toxic chemicals, precise alignment equipment that are typical of optical lithography. Additionally, it allows high geometrical freedom, high lateral and vertical resolution, fast laser processing of the material without contacting it, the formation of patterns (including channels) with different depth and width, processing of thicker materials in a reasonable time scale (less than 24 h), large substrate area processing, mass production of custom-designed features with precise alignment and length-scale from μm to nm and laser engraving in ambient air (no controlled environment needed) [20,24]. Glass micromachining can be accomplished based on a wide range of wavelengths (ultraviolet to infrared) and pulse width (micro-to femtosecond) [26–30]. The primary requirement to be fulfilled for successful laser ablation-induced machining is strong absorption of the material to be processed at the laser operating wavelength, with micrometer-scale absorption depth in the material. Ultrafast picosecond laser was demonstrated as a valuable tool for direct cutting, drilling and micro-machining of glass as well as for glass-to-glass bonding without adhesive layers [31]. Despite excimer ultra-short (i.e., pulse width in the femtosecond to picosecond range) lasers provide high-precision material processing with crack- and almost debris-free surfaces and high precision profiles with respect to nanosecond or longer laser pulses [32–34], the related highly expensive instrumentation favored spreading use of economic (relatively simple equipment and low capital investment) microsecond-pulsed carbon dioxide (CO_2) laser sources operating at wavelengths strongly absorbed by glasses [28,30,35]. Hence, although limited to the realization of micro-sized structures (since heat dissipation in the surrounding material during the photo-thermal process influences the spatial resolution), nowadays CO_2 laser–based ablation/micro-machining represents a serial method to engrave patterns on glass materials (such as quartz, borofloat and pyrex) [35] that have found applications in solar cells to enhance light trapping efficiency [36].

Since interaction of long-pulse lasers with materials causes thermal-regime ablation with heat conduction beyond the laser irradiated region (photothermal ablation-regime), extended heat affected zones, redeposition of melted droplets and debris (recast) formation around the side walls of the laser-processed region (grooves, trenches, holes) can be observed. All of this may impact on bonding the laser processed glass workpiece. Therefore, when using CO_2 laser sources, high surface quality micro-machining on glasses demands on optimizations of the main laser and processing parameters as well as proper choice of the glass material [35,37].

Hence, inspired by the possibility of producing fast low cost LoCs, OoCs and other microfluidic devices as well as masters for patterned substrates, in this work, we implement the fabrication of quartz microstructures using micro-second pulsed CO_2 laser-based ablation. Among various glasses, we focused our attention on quartz since it is the hardest substrate to be etched via wet chemistry [38] and it appears the most stable to ablation by long-pulse lasers.

Thanks to the versatility of the method, trenches/grooves and holes with different depth, shape and lateral dimensions were produced on the same workpiece. This is an important practical advantage of the CO_2-laser engraving technique. Indeed, the mass production of different depth micro-structures by conventional lithography approaches usually require complex and multi-step processes.

Micro-structures of hundreds of microns were laser-ablated at room temperature within (22 ± 2) °C, (estimated etching rate of 34 μm/s) without the need of reagents-resistant masks, followed by a 2h lasting post-ablation wet etching to remove residual ripples and rims stemming from the thermal-ablation regime. The structures produced by laser ablation were assessed in terms of specific applications: the grooves as multi-channels to fabricate microfluidic reactors [6,39,40] and the micro-holes as molds for micro-pillars enabling studies of 3D cell cultures [41,42]. To the best of our knowledge, these are the first examples of CO_2 laser-engraved serpentine quartz micro-reactors reported in the literature. On the other hand, the ablated micro-nozzles were unconventionally used to realize an array of micro-pillars in Cyclic olefin copolymer (COC) over a large area. Due to its advantage in terms of high mold detail replication, COC was used as a template for promoting cells growth and self-assembly depending on the laser-related surface characteristics of the COC micro-pillars. This aspect is of applicative interest because endothelial cells (ECs) were found to organize around such micro-pillars, thus suggesting a micro-vessel-like assembly, which is interesting in the view of producing OoC models for in vitro drug assays or study of cardiovascular diseases.

2. Materials and methods

2.1. Materials

B270, BorofloatTM (BF), pyrex, soda-lime, quartz substrates were provided from Telic (USA) and from Pearl-Vemi. COC (Topas 8007S-04) substrates were purchased from TOPAS Advanced Polymers, Inc. Sylgard-184, PDMS elastomer, was purchased from Dow Corning (USA).

Human Umbilical Vein Endothelial Cells (HUVECs) were provided by PromoCell. 4-(2-hydroxyethyl)-1-piperazineethanesulfonic acid (HEPES), Endothelial cell growth supplement from bovine neural tissue, Heparin sodium salt, Phosphate-buffered saline (PBS), formaldehyde, Phalloidin-TRITC, 4,6-diamino-2-phenylindole (DAPI), Hydrofluoridric acid (HF), Hydrochloric Acid (HCl), ammonium fluoride (NH_4F) to produce buffered oxide etchant (BOE) solution [43], acetone and isopropyl alcohol (IPA), ethanol, eosin, sulfuric acid (H_2SO_4) and hydrogen peroxide (H_2O_2) were purchased from Sigma-Merk; Fetal Bovine Serum, Penicillin-Streptomycin, glutamine, Trypsin-EDTA solution were purchased from Corning, fibronectin from Santa Cruz Biotechnology, Triton X (Triton™ X-100), serum albumin in PBS (Blocker™ BSA) and ZO-1 Monoclonal Antibody Alexa Fluor 488 from Life technologies.

2.2. Laser setup and processing parameters

All ablation/engraving experiments were performed by using a commercial laser engraver (Trotec Laser Speedy 360 Flex https://www.troteclaser.com/en-us/laser-machines/laser-engravers-speedy-series/) equipped with a CO_2 laser source operating at 10.64 μm wavelength and with a pulse width $\tau_p = 1000$ PPI (pulse per inch).

Fig. S1 presents a scheme of the scanning strategy and processing parameters. The laser beam, focused using a lens with a focal length FL = 38.1 mm, was guided over the workpiece surface according to a computer controlled 2D scanning pattern consisting of several roundtrip lines properly displaced with respect to each other (see Supporting Information, section "S.1 Laser processing parameters and scanning method"). The glass workpiece was stationary in XY and was moved in Z in order to optimize dynamically the focus. Laser beam was moved using an optical fiber. The fiber was mounted on a pantograph with high precision brushless DC electric motor. The laser beam was scanned using average laser power values $P_{avg} = 10, 15, 20, 25, 30, 35, 40, 45, 50$ W. The beam scanning speed (v_s) was set at the values $v_s = (c^* v_{max})/100$, where $c = 2.5, 3, 5, 7, 7.5, 10, 15$ and $v_{max} = 355$ cm/s is the maximum scan speed. Hence v_s varies over the range 3.6–53.3 cm/s. Hereafter, scan speed will be referred to as the value of c briefly. Pulse repetition frequency (f_{rep}) was set to 1000 Hz.

On the basis of the experimental procedure (Fig. S1(a)), the operating

parameters can be classified in two categories, that is, parameters of the focused pulsed laser beam (laser parameters) and parameters of the scanning process (process parameters). The former group includes average power per pulse (P_{avg}), pulse width (τ_p), beam diameter (D_S), pulse repetition frequency (f_{rep}), and fluence (F) that can be expressed by the relationship $F = P_{avg} * \tau_p = E_p/A_s$, where A_s is the spot area and E_p is the pulse energy per unit surface. The scanning process is characterized by the scan speed (v_s), the scanning distance ($d_{pp} = v_s/f_{rep} < D_S$), representing the spacing between subsequent laser-pulse spots along the scanning direction *x* (that is a measure of beam overlapping along the scanning direction), the track pitch ($d_{track} < D_S$) that represents the spacing between parallel neighbor ablated traces (which is a measure of beam overlapping perpendicularly to the scanning direction), the number of pulses per inch (PPI) and number of back/forward iterations of the laser beam along the same scanning line (N_{step}). Also, the thermophysical properties of the workpiece to be laser-processed play a role. As thermal conductivity determines the rate of heat spreading far from the initially laser-irradiated localized region, high thermal conductivity results in a deeper cut.

The final ablation depth, defined as the height difference between the initial surface and the bottom of the engraved/drilled structure, is function of F, d_{pp}, d_{track} and N_{step}. Noteworthy, for a given laser power, calculation of fluence requires accurate knowledge of the laser spot size. Unlike the theoretical diameter of the laser beam, the experimental one may increase with increasing laser power due to Gaussian approximation of the laser beam intensity distribution. Gaussian profile means that energy pulse is maximum at the beam centerline and decreases radially when moving away from the centerline and the incident beam diameter is defined as the diameter when the energy drops to ($1/e^2$) [44]. Moreover, upon increasing the number of laser passes, increasing depth of the groove causes out of focusing of the laser beam at the incidence surface. Therefore, since a constant diameter spot may not be assumed in experiments varying the laser power and involving iterated laser passing along the scanning direction, poor control on fluence may result, meaning that the nominal fluence value may differ from the actual one.

Engraving of channels being an accumulating (on the same site and under iteration) ablation process, the ablation rate and photothermal mechanisms also depend on the morphology modifications under iterated laser irradiation and overlap between contiguous grooves. Hence, trench width and edge shape depend not only on the delivered energy but also on the effective beam overlapping ruled by laser spot-size, scanning speed, pulse frequency and $d_{track} << D_S$. On this basis and accounting for the different morphologies (trenches, circular and square holes) discussed in this study, hereafter, in addition to detail the processing parameters set in experiments, we consider linear energy density, defined as laser power divided by scanning speed ($P = P_{avg}/v_s$).

The described experimental set-up was applied to carry out the different sets of micro-scale structures sketched in Fig. S1(b): i) 4 mm long micro-channels of 200 μm nominal width with interline of 400 and 600 μm, and ii) square/circular micro-holes with nominal edge/diameter of 500 μm and center to center distance (pitch) P = 400, 500, 600 μm.

2.3. Post-ablation treatments and morphological characterizations

Following laser-based engraving of the micro-structures, a quartz etching processing was performed by the BOE solution, consisting of 1.38 M NH_4F dissolved in pure water with addition of HF (48%) and HCl (38%) to obtain HF: NH_4F: HCl 1:41:1 ratio. The substrates were incubated in BOE solution for 2h under sonication and then washed with pure water to remove residuals of the ablation process. On the other hand, as-ablated quartz samples (not treated with BOE solution) were used as molds to produce COC micro-structures by hot embossing. A COC flat substrate was treated under a hydraulic press (PW 40H from P/O Weber) using the ablated quartz as mold at 100 °C and P = 15–25 KN for 10 min.

The depths of the micro-structures in quartz and the heights of the COC micro-pillars were calculated using the profilometer Dektak 6 M Stylus Profiler (Digital Instrument-VEECO). The lateral dimensions and the optical images of the samples were obtained by an inverted optical microscope system (NIKON Eclipse Ti). The values reported in the graphs are an average over 3–6 structures and the uncertainty was calculated as standard deviation. As further morphological studies, Scanning Electron Microscope (SEM) images of the COC micro-structures were acquired at low energy 5 KeV (SEM, Carl Zeiss Merlin). A thin metallic layer (about 3 nm of chromium and 5 nm of gold) was thermally evaporated on the COC molds to prevent sample charging throughout electronic scanning.

2.4. Fabrication and performance test of the microfluidic reactors

Laser ablation technique was used to produce three serpentine micro-reactors of different internal volumes (see Video S1). The engraving parameters were: P_{avg} = 40 W, v_s = 15, N_{step} = 15, f_{rep} = 1000 Hz. The geometry of the micro-reactors was designed using Solidworks (Dassault Systèmes, France) computer-aided design software. Mixing of two different fluids occurred in the serpentine after injection from two inlets through the T-shaped channels. The three serpentine reactors, shown in Fig. 1 (a), have a nominal channel width of 250 μm and a length of about 280, 390 and 850 mm. After fabrication, the reactors were treated with BOE solution for 2h under sonication and then washed by pure water as reported in par. 2.3. Then, a 4 mm thick PDMS layer was prepared by polymerization of the mixture pre-polymer/curing agent (10:1 ratio) at 140 °C for 15 min. Three holes of 1.5 mm diameter were punched using a biopsy puncher at distances corresponding to the micro-reactors inlets and outlet. To assemble the quartz moieties of the serpentine micro-reactors with the flat PDMS slides, the mortar layer method was used [45]. A 10 μm thick layer of PDMS diluted in toluene (4:1 wt%) was deposited by spin coating on a glass substrate (first cleaned with acetone and IPA, dried by N_2) [46]. The quartz micro-reactors were cleaned by piranha solution (H_2SO_4:H_2O_2 3:1) for 1 h, washed by pure water and dried by N_2. The PDMS slide with punched holes was washed with ethanol, dried by N_2 and put in contact for 10 s with the PDMS uncured layer deposited on glass. Then the quartz moieties and the PDMS slides were aligned and bonded at 140 °C for 15 min in oven. After bonding, the micro-reactors were tested by flowing pure water and eosin in water from the two inlets at different flow rates (10, 20, 50, 70, 100, 150, 200, 300 and 500 μL/min) for 5 min to evaluate the stability of the sealing. The flow rates were set by a double channel syringe pump (Ugo Basile, Biological Research Apparatus, model KDS270). The chips were connected to tubings (Tub Tfzl Nat 1/16 x 0.40, IDEX-HS) by fitting the two micro-reactor inlets through the needles of the syringes (see par. 3.2.1).

Supplementary data related to this article can be found at https://doi.org/10.1016/j.mtbio.2021.100163.

2.5. Culture of ECs using micro-pillars as templates

HUVECs were sub-cultured on flask with medium 199 (with 25 mM HEPES) supplemented by 50 μg/ml EC growth supplement from bovine neural tissue, 20U/ml Heparin sodium salt, 15% Fetal Bovine Serum, 50U/ml and 50 μg/ml Penicillin-Streptomycin, 2 mM L-glutamine. ECs were maintained in a humidified CO_2 incubator at 37 °C and 5% CO_2, replacing the medium every 3 days. Passage 4 HUVECs were used in the experiments on COC micro-pillars and flat COC substrates. COC samples were coated with 5 μg/ml human fibronectin solution for 1 h at 37 °C and rinsed with PBS solution. HUVECs were 90–95% of confluency in a T25 flask, detached using 0.05% Trypsin-EDTA solution and split 1:1 on COC substrates placed in dishes. Dishes were incubated for 2 h to allow cell adhesion and subsequently, COC substrates were moved in new dishes with fresh medium. Dishes were maintained for 1 week in a humidified CO_2 incubator at 37 °C and 5% CO_2, replacing the medium every 3 days. After growth, the cells on COC samples were fixed with 3.7% formaldehyde for 15 min at room temperature (RT) to perform immunocytochemistry. After permeabilization in 0.1% Triton X in PBS for 10 min, the samples were blocked with 1% Blocker™ BSA for 30 min at RT.

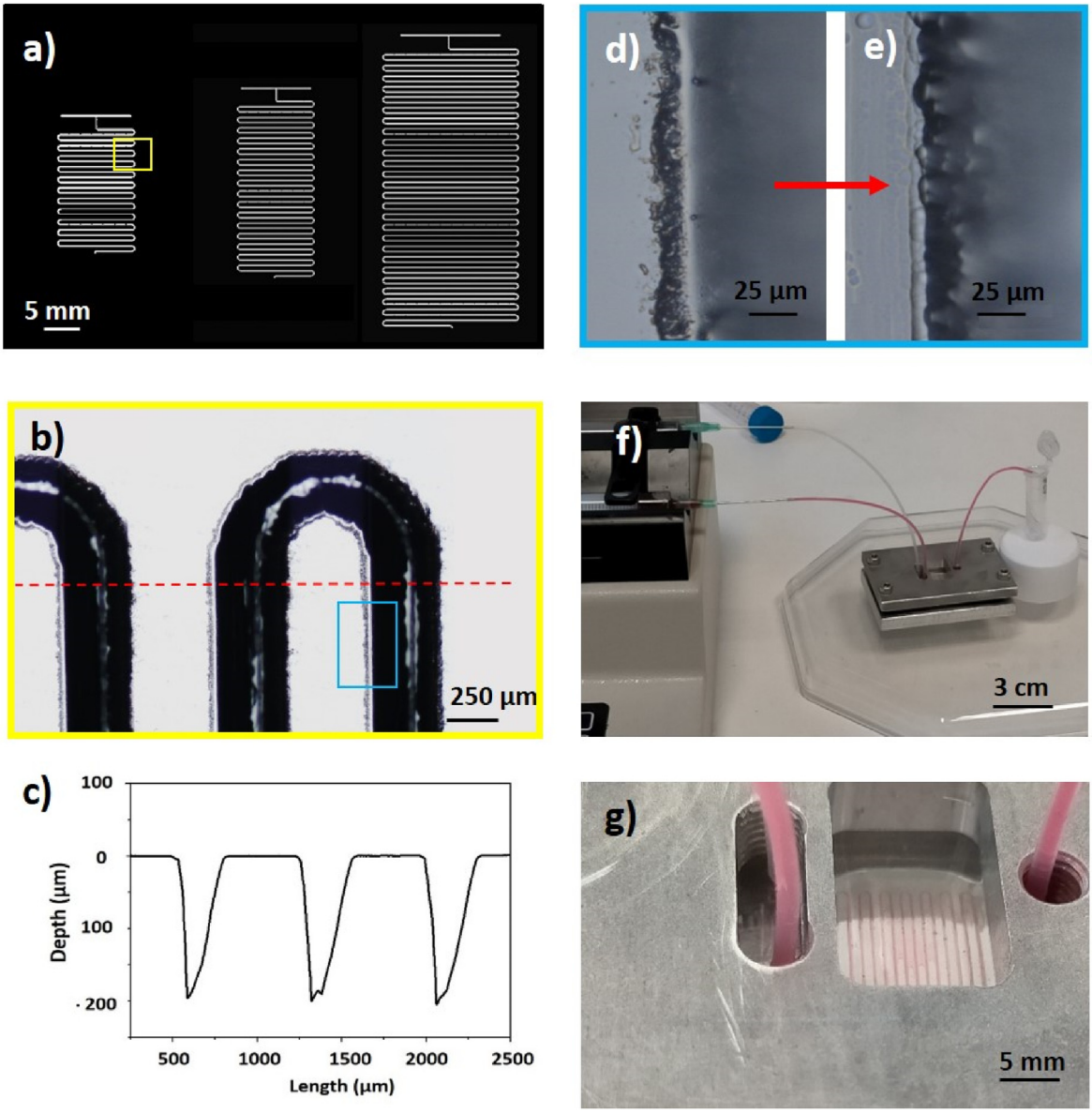

Fig. 1. Imaging and characterization of serpentine-like micro-channels manufactured by CO_2 laser-ablation at $P_{avg} = 40$ W, $v_s = 15$, $N_{step} = 15$, $f_{rep} = 1000$ Hz. a) Drawing of the three fabricated micro-reactors with the yellow box indicating the area of the serpentines imaged by optical microscopy; b) optical image of the detail of the serpentine micro-channel before the BOE treatment in the area pointed out in panel (a) by a yellow box. The red dashed line represents the cross section along with the profilometer analysis was performed. The cyan box is an area where rims are well visible along the channel edges. (c) Profilometer line of three micro-channels treated by BOE solution along the direction indicated by the red dashed line in Figure (b). Optical images of micro-channels before d) and after e) 2 h of wet etching in BOE solution under sonication. f) Picture of a micro-reactor connected to the syringe pumps during injection of the eosin solution (pink solution) and pure water. g) Picture zooming the micro-reactor area with focus on the serpentine and the mixing process. (For interpretation of the references to colour in this figure legend, the reader is referred to the Web version of this article.)

Subsequently, the samples were incubated with 1 µg/ml of ZO-1 Monoclonal Antibody Alexa Fluor 488 for 1 h at RT, washed three times with 1% BSA in PBS. For staining of F-actin, Phalloidin-TRITC was used at a concentration of 2 µg/ml in PBS. Nuclei were counterstained with DAPI and stored in PBS before imaging. Images were captured with a Nikon Eclipse Ti microscope.

3. Results and discussion

In our experiments the glass material of choice is quartz due to its superior optical transparency with respect to other glasses, allowing clear visual inspection of the working microfluidic platform and fluorescent probes in LoCs/OoCs, smooth surface of the trench bottom as well as absence of cracks and good quality profile of the channel trench [23,47,55]. In this respect, it is worth observing that high temperature gradients combined with a relatively high thermal expansion coefficient and low heat conduction favor the generation of thermal strain and stress induced-micro-cracks during laser photo-thermal processing [48–50]. Additionally, the quartz is more difficult than other glasses to be etched with both wet or dry methods [51,52], which makes CO_2-laser ablation an appealing perspective for deep (≥100 µm) engraving of quartz workpieces.

For the sake of completeness, we also investigated other glass substrates such as soda-lime, pyrex, B270 and BorofloatTM. Power thresholds and etched depths were expected to be dependent on the physical/chemical properties of the glasses because of different laser-material interactions that determine different melting and vaporization processes [53]. Indeed, we observed critical aspects such as the occurrence of

extended heat affected zones, cracking, rough surfaces and limited processing conditions (see Supporting Information, section "S.2 Ablation of different glass substrates") in the case of all the investigated glasses except quartz, that exhibited the best performances in terms of quality of both trench and hole profile. Therefore, hereafter our experiments and discussion will focus on CO_2 laser processing experiments of quartz.

Noteworthy, in this study we do not present a systematic investigation of the influence of all laser and process parameters on the engraved feature in quartz substrates because this aspect was already widely investigated in the literature [35,54–58]. However, we performed calibration experiments (see Supporting information, section "S.3 Laser-engraving calibration experiments") to optimize the laser processing conditions in perspective of fabricating micro-channels useful for microfluidic highly optically transparent platforms and to assess the experimental parameters to produce micro-holes acting as molds in manufacturing micro-pillars for several applications. According to this aim, we designed our experiments to obtain low aspect ratio and controllable shape micro-structures, meaning the ablated depth doesn't need to be maximized and distortion effects of the ablated profile under deepening have to be avoided [57]. As main outcomes, we observed that at linear energy density $P \geq 0.75$ J/cm and $N_{step} > 15$, the depths of the engraved micro-structures (micro-channels and micro-holes) are significatively different as result of different mechanisms of heat dissipation in confined environments (see Supporting information, section S.3). Furthermore, high scan speed v_s was found to reduce significatively lateral enlargement effects that increase the nominal size of the designed micro-structures.

3.1. Removal of ripples and rims by a wet/chemical approach

Beyond the formation of rims due to heat diffusion of the energy delivered to the irradiated material outside the irradiated spot, the morphology of the micro-structures can be affected by the formation of ripples generated during processing over parallel tracks (Fig. S1(a)). Ripples stem from the stepping-motor-driven translation of the laser beam at the corners and arcs of the pattern and their formation is indicative of an accurate reproduction of the beam scanning process. Their characteristics also depend on the morphology of the ablation traces as determined by the degree of overlap of the ablation micro-grooves/spots of subsequent laser pulses and number of passes. In general, scribing a channel requires a sequence of overlapping ablation craters yielding a continuous rather than intermittent track. Above the ablation threshold, ejection of vaporized material as well as melt and clusters occurs due to intense heating of a limited volume and pressure shockwave-induced melt recoil, ejection and splashing outside the ablation groove.

While engraving a linear trench, heat affected zones run parallel to the channel profile and eventual re-solidified melt splashes or fibers occur at the trench edge. Optical microscope analysis in Fig. S7 shows how the interplay between the occurrence of rims and ripples along the y direction affects the morphology of the processed structure for varying number of steps (Fig. S7(a)–(f), $N_{step} = 5$, 10, 15, 20, 25, 30) and laser power (Fig. S7(g)–(k), $P_{avg} = 30$, 35, 40, 45, and 50 W). It can be clearly observed that for given $P_{avg} = 40$ W and $c = 15$, increasing number of laser passes favors more extended heat affected zones as well as severe deterioration of the ripple morphology for steps larger than 15, with the presence of re-solidified melted material and fine particles. For given $c = 15$ and $N_{step} = 15$, increasing P_{avg} has less impact than the previous situation. This result can be explained based on decreasing fluence, according to the above discussion. Consistently, small fragments (indicated by the arrow in Fig. S7 (k)) close to the ripple edges, stemming from re-deposition of small melt droplets and/or condensation from the vapor phase and/or temperature gradients versus depth, indicate less effective heat and pressure induced explosive mechanisms.

From the applicative standpoint, the presence of both rims and ripples may be critical in perspective of manufacturing microfluidic platforms by sealing the ablated structures to other patterned or un-patterned substrates. In particular, for the applications of interest in our study, ripples are highly undesirable because they occur along the entire length of the micro-channel walls. Considering that laser ablated quartz has a different reactivity towards chemicals than untreated one [59], an attempt to remove rims/ripples was performed to allow easy bonding to other substrates [35] in the perspective of producing sealed micro-channels.

A post-laser processing wet etching was performed by exposure to the BOE solution, that is used for chemical etching of various glass substrates [11,60]. Optical imaging results of the optimized procedure are reported in Fig. 2 (a)-(f), where the BOE-untreated micro-structures are also shown for comparison. Before etching by BOE solution, ripples are clearly visible for any geometry of the micro-holes. Following the etching treatment, both ripples of the micro-holes and rims along the channel edges were clearly reduced. Profilometer measurements also confirm that the BOE treatment acts on the ripples positively (see Fig. 2 (g)) and smooths the debris caused by the laser ablation process. Indeed, by zooming the profile of a micro-structure acquired along the x axis length, a clear reduction of the thickness of the lateral ripples at the edges of the crater (as indicated by the green arrows) is observed by comparing the profile before (black line) and after BOE treatment (red line). Furthermore, BOE was found to be unable to etch laser-untreated quartz in the current experimental conditions (see par. 2.3).

By comparison, wet etching of the groove profile of CO_2-laser treated silica glass is reported by using an etchant solution with 3.6% HF and 18% NH_4F by volume [61]. In this study, it was observed different etching rate between the laser-treated and untreated glass [61]. Differences in the etching effectiveness by BOE between quartz and silica glass can be ascribed to the relevant structural differences, that is covalently bounded crystalline quartz and amorphous silica glass. On the other hand, depending on fluence, laser-induced high temperature heating of quartz yields a loss of oxygen as well as changes of the chemical structure of untreated quartz consisting of the formation of quartz polymorph phases with lower O1s–Si2p binding energy (i.e., increased Si–O–Si angle) than untreated quartz [62]. These modifications are expected to be responsible of the different etching ability of BOE with respect to laser-treated and untreated quartz.

The applied etching procedure also acts on both walls and bottom of the structures, where laser-induced heat affected zones occur [61]. In particular, as a result of BOE etching of the prepared micro-structures, it was observed a consistent increase in the micro-channel depth (changing from (143.5 ± 2.7) μm before etching to (163.2 ± 3.3) μm after etching) and a minimal increment in the micro-holes depth (from (129.7 ± 1.7) μm before etching to (130.2 ± 3.3) μm after etching). This experimental finding would indicate the occurrence of larger heat affected zone in the case of the micro-channel that favors progressing of BOE etching over a larger distance. In this respect, it is reasonable to assume that engraving a micro-channel result in more thermal gradient effects and thermal losses by conduction around the laser irradiated volume than a micro-hole.

Hence, the production of quartz micro-channels and micro-holes and an accurate removal of the ablation-induced rims and ripples were obtained by an easy and low cost approach by combining wet etching with optimization of the laser processing of any geometrical structure. We calculated that micro-structures of hundreds of microns were engraved at room temperature within (22 ± 2) °C with an etching rate of 34 μm/s, without the optimization of high reagent-resistant masks, the use of expensive equipment and clean room facilities. After ablation, the quality of the micro-structures was improved by a 2 h wet etching at room temperature. This result is not trivial considering that wet etching of fused silica proceeds at etch rate of 340 nm/min at 47 °C using standard mask conditions [51,52] with improvements up to 1 μm/min at RT only in presence of specific masks formed by single-coated silicon-based thin film [38]. On the other hand, plasma dry etching that requires expensive equipment and high-selectivity masking material, results in etching rates <190 nm/min [63].

Definitively, CO_2-laser engraving is an effective micro-patterning

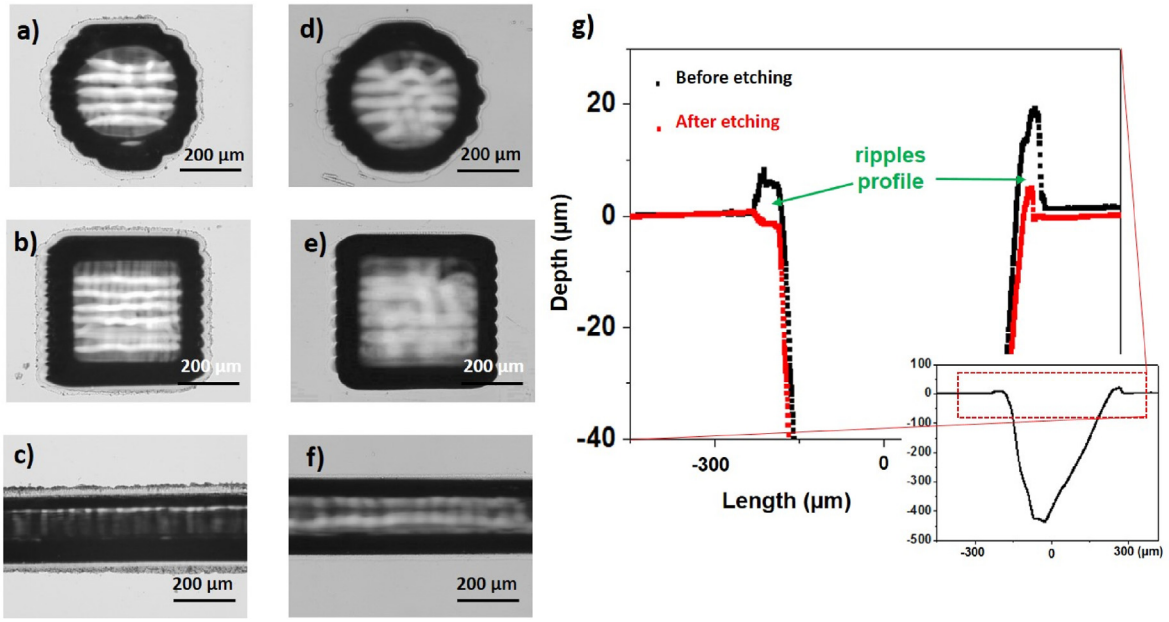

Fig. 2. Optical images showing circular, square holes and micro-channels before a), b), c) and after d), e) and f) 2 h of wet etching in BOE solution under sonication. g) Analysis at the profilometer of the ripples before and after etching. The micro-structures have been ablated at $P_{avg} = 40$ W, c = 15, $N_{step} = 10$.

approach of quartz enabling fast and flexible production of features with different size, shape and control on the design process.

3.2. Application examples

3.2.1. Microfluidic reactors

An applicative example of the CO_2 laser-based engraving in microfluidics is the manufacturing of serpentine-like micro-rectors, in which diffusive mixing at low Reynolds number regimes is enhanced by an engineered velocity profile [64].

The experiments reported in par. 3.1 and in section S.3 of Supporting Information allowed to select some relevant parameters to engrave micro-channels of suitable length and width to produce micro-reactors. In particular, to promote fluid mixing micro-channels of depth around 200 µm with a serpentine geometry and T-shaped converging fluid inlets were manufactured (Fig. 1) by setting $P_{avg} = 40$ W, c = 15, $N_{step} = 15$ and $f_{rep} = 1000$ Hz (see Fig. S6 (e)). The three micro-reactors under consideration (Fig. 1 (a)) have an internal volume of about 18, 25 and 55 mm^3 respectively and micro-channels with an average width of (324 ± 9) µm as calculated by optical images (Fig. 1 (b)).

As expected, residuals of the thermal-character of the ablation process are present along the channel edges as marked by the cyan box in Fig. 1 (b). Fig. 1 (c) shows the spatial profiles of the micro-channel cross section measured by the profilometer along the scan direction defined by the red dashed line in Fig. 1 (b). The engraved structures resulted very repeatable. Noteworthy, since the profilometer analysis shown in Fig. 1 (c) was acquired after BOE treatment performed according to the guidelines above discussed, it didn't show any debris at the edges of the micro-channels, thus confirming the efficacy of the BOE treatment. Removal of rims by BOE-based etching (Fig. 1 (e)) was necessary to avoid the failure of sealing of the serpentine micro-channel to other layers during the assembly of the micro-reactors. For comparison, the unsealed serpentine micro-channel before the BOE etching shown in Fig. 1 (d) exhibited irregular lateral profiles that could be observed by optical inspection.

After the detailed preliminary studies and treatments, a hybrid micro-reactor formed by quartz and PDMS was assembled. An un-cured PDMS thin layer was used as glue between the quartz and the PDMS substrate. An optimization of the thickness of such a layer was performed to allow sealing without channel occlusion. Before sealing, three holes located at suitable distances were punched on PDMS to allow flow injection and collection. Fig. 1 (f) shows a picture of a serpentine micro-reactor connected to the syringe pumps during injection of the eosin solution (pink solution) and pure water. Fig. 1 (g) zooms the micro-reactor area pointing out the serpentine geometry and the mixing process.

The micro-reactors were tested to check their stability during the flow in a range of conditions suitable for performing chemical reactions [65–67]. From the two inlets, two solutions of pure water and eosin (the pink solution in Fig. 1 (f) and (g)) were injected first at flow rates of 10 µL/min for 5 min from both inlets, then they were gradually increased to 20, 50, 70, 100, 150, 200, 300 and 500 µL/min. Hence, the micro-reactors were pressured for 45 min at growing flow rates up to 500 µL/min (corresponding to 1 mL/min of overall volumetric flow rate) without observing any leakage. These flow tests demonstrate that the post-ablation BOE treatment is efficient in selective removal of rims/-ripples (no alteration of un-treated quartz areas was observed) that is necessary to seal ablated quartz substrates to other surfaces for micro-reactors assembly.

Beyond hybrid quartz/PDMS micro-reactors, the method can be extended to assemble quartz-quartz micro-reactors by fusion bonding [68]. Compared to PDMS micro-reactors, quartz-based micro-reactors are superior in terms of stability to aggressive chemicals, high temperature and mechanical/flow stimuli. Indeed, since PDMS swells in many organic solvents, the applications of PDMS micro-reactors are mainly restricted in aqueous environment [69,70]. Furthermore, glass micro-reactors are stable at pressure up to 4 x 10^7 Pa [71] and at high temperature (fusion bonding of two glass substrates occurs between 600 and 900 °C). On the other hand, delamination of PDMS micro-reactors is observed at pressures around 0.02–0.03 x 10^7 Pa [72,73], and thermal processing lead to changes of the polymer stiffness [74] and, above 400 °C, to polymer degradation [75]. A further practical issue that cannot be ignored is that connections to the tubings are more stable for the glass micro-reactors than for the PDMS micro-reactors (glue adhesion on glass is stronger than on PDMS). Additionally, quartz micro-reactors have a wide optical transparency in the UV spectral range and are less susceptible than PDMS to (bio)molecular adhesion; hence, they can be more easily cleaned with a variety of solvents and used several times even for different processes.

Therefore, considering all these advantages, quartz micro-reactors

may find a wider range of applications compared to PDMS micro-reactors.

3.2.2. 3D cell culture templates

In the perspective of future applications of the etched micro-structures beyond microfluidics, we investigated the possibility of exploiting the ablated structures as master providing a new, simple and fast method to fabricate micro-pillars with different shape. Micro-pillars are often produced because of their applicative interest as filling material for micro-columns [76,77] for applications in plasmonics or photonics [78,79], or for other advanced functions of LoCs [53,61]. Moreover, micro-wells with variable shape and depth were studied to allow 3D cell culture in the form of spheroids or organoids [80,81].

In applications where cells cover surfaces, as in the case of OoC models of capillary vessels, it is worth studying the impact of surface curvature on cell adhesion, interaction and growth. For instance, ECs of the vascular system are generally elongated and align along the direction of blood flow to optimize their functions [82,83]. Collective behavior of cell assemblies, as a function of the substrate topography, and of their proliferation and adaptation to various adhesion surfaces differing in structure and composition are critical investigations in biology and medicine. In particular, in order to gain understanding of the cell behavior on a microscopic scale, spreading and proliferation of cells were extensively investigated on high-density micro-pillar arrays [83–86]. In this framework, micro-patterning techniques [84,87] providing structured features with the length scales of the cell interaction and usage of non-toxic materials are demanding.

A micro-structured mold can be used for fabricating microfluidic devices and micro structured arrays of different polymeric materials such as PDMS, PMMA and COC. Whereas PDMS is particularly suitable to develop microfluidics devices as well as architectures for the incorporation of cells and high aspect ratio micro-pillars [88], major disadvantages are its adsorbing small hydrophobic drug molecules [89,90], the release of uncrosslinked oligomers and the need of developing protein coatings for applications in tissue engineering. Among the most common materials used for LoC and OoC applications, COC was demonstrated to be highly resistant to organic solvents (Topas Advanced Polymers 2009 and Zeon Chemicals 2009 from Ref. [91]) and suitable for biomedical applications, thanks to its biological inertness [92,93] and its low water absorption that poorly affects the environmental conditions of cell living and interaction [94]. Moreover, COC is also highly transparent in the visible and near ultraviolet regions of the spectrum, hence being interesting for optical components [95].

The main low-cost production and fast prototyping techniques to manufacture COC are hot embossing, injection molding and nanoimprint lithography (NIL) [96–98].

In this work, COC micro-pillars of conical and square pyramidal shape were produced by hot embossing from a quartz mold. The processing pressure and temperature were optimized to allow the correct replicas of the ablated holes. The fabrication accuracy and morphology of the COC microstructures at the nanoscale were evaluated by SEM (Fig. 3).

Features due to the laser machining over parallel tracks are more visible at low number of steps (5 steps in the case of Fig. 3 (a) and 3 (b)) and less visible for increasing number of passes (15 steps in Fig. 3 (c) and 3 (d) and 20 steps for the structures shown in Fig. 3 (e) and 3(f)). Indeed, iterated laser induced local melting is expected to modify the surface morphology of the irradiated surface. So higher number of steps decreases the roughness of the final structures.

Tilted SEM images were also acquired with the aim of defining the 3D shape of the molded structures (see images of Fig. 3(c) and (d)). The

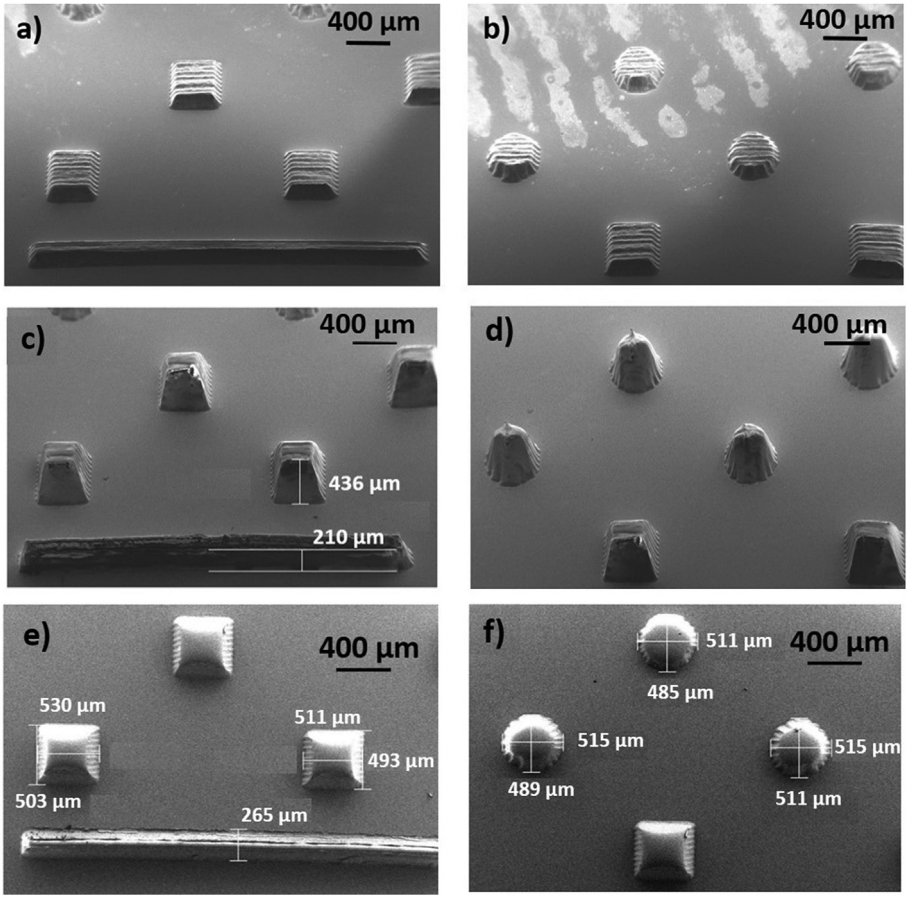

Fig. 3. SEM images of conical, square pyramidal structures in COC obtained by molding from ablated quartz micro-holes produced by treatment at c = 15 and a) b) P_{avg} = 40 W, N_{step} = 5 (tilted-view); c) d) P_{avg} = 45 W, N_{step} = 15 (tilted-view); e) f) P_{avg} = 40 W, N_{step} = 20 (top-view).

obtained protrusions clearly demonstrate the Gaussian-like profile of the laser-processed structures, although with some deviations induced by high aspect ratio and/or re-deposition or re-melting on the groove walls. The micro-structure height (Fig. 3(c)) was also assessed by leveraging SEM analysis, however an overestimation with respect to the values achieved by profilometry technique of Fig. S6 is appreciable. Actually, despite tilting correction, the SEM inspection is strongly affected by the gaussian-like profile, thus the profilometer values were considered more reliable. It is worth noting that the lateral size of the micro-structures as calculated by SEM and by optical inspection revealed the asymmetry of the micro-structures with L_x sizes (along the scan direction) larger than L_y ones (see Fig. 3 (e) and (f)).

As an intriguing application of the fabricated COC micro-pillars, we tested their capability of driving cell growth in a 3D configuration. In particular, we aimed at self-assembling HUVECs to produce segments of human blood vessels oriented perpendicular to the surface. This arrangement could be interesting for some OoC applications in which microfluidic lumen-based systems are used as models to recapitulate the anatomy and physiology of tubular organs [99]. On this basis, the micro-pillar arrays under consideration are spaced over a large area, with width and height of hundreds of micrometers rather than a few micrometers, as commonly reported in the literature.

Although femtosecond laser ablation was already used to engrave scaffolds of polylactic-co-glycolic acid [100], it was only demonstrated the organization of bovine endothelial cells in branched micro-vessels oriented parallel to the scaffold plane without reporting observation of the cross section of a vessel as well as a comprehensive study of the 3D cellular organization [100]. In other works, bovine aortic endothelial cells were reported to grow more successful on high-density silicon micro-pillars than on flat silicon wafers with a tendency to mechanically relax around the 3D topography [101].

Here, the HUVECs were seeded on both COC micro-pillars oriented perpendicular to the surface and flat COC substrates. Results are shown in Figs. 4–5. Fluorescence images of the three channels phallodin-TRITC (red, Fig. 4 (a)), DAPI (blue, Fig. 4 (b)), and zonula occludens-1 (ZO-1) (green, Fig. 4 (c)) were used to stain cytoskeleton (TRITC), nuclei (DAPI) and to evaluate the expression of tight junctions (TJs) between the cells (ZO-1). HUVECs assembled in a very compact way around the micro-pillars since they formed a TJs network as ZO-1 expression reveals (see Fig. 4 (c)). Noteworthy, the same experimental finding occurs for all the isolated pillars of the array, which indicates a repeatability of the observed cell wrapping and its being strictly related to the micro-structuring of the substrate. On the contrary, HUVECs growing on a flat COC substrate did not express ZO-1 protein and had a typical cobblestone-like morphology (see Fig. 4 (d), (e), (f)). These results are quite interesting, in view of developing vessel-like networks of HUVECs.

Indeed, although the fluorescence images are not tridimensional, they show the projection of the lateral surface of the micro-pillars on the substrate. Hence, according to the following reasoning, the lateral walls of the conical and square pyramidal pillars are surrounded and wrapped by the cells. The black regions of the optical images reported in Fig. 5 (a), (b) (left side panels) correspond to the walls of the pillars in the 3D SEM images of Fig. 3, that are not perpendicular to the surface, due to the conical or square pyramidal shape of the corresponding quartz micro-holes produced by the laser ablation. Hence, Fig. 5(a), (b) suggest that the black regions around the two circular or square planes, representing the basement and the top of the micro-pillars respectively, are filled by cells that strongly interact each other and tend to distribute closer to the micro-pillar edges. Further hint to this statement can be found by combining information stemming from micro-fabrication and cell culture. As Fig. 5 (c), (d) show, the thickness of the fluorescent area becomes larger for pillars obtained by quartz molds ablated under increasing fluence (P_{avg} = 35 W, in Fig. 5 (c) and P_{avg} = 40 W in Fig. 5 (d)). According to the developed discussion about laser engraving (Fig. S6 and Fig. 3), increasing fluence (by increasing the linear energy density P at constant v_s) causes both deepening of the micro-holes and deviation of the lateral walls from the vertical direction. Both effects yield higher and more conical/square pyramidal pillars, which results in increased area of the projection of the lateral surface of the micro-pillars on the substrate. Hence, if cell wrapping occurs around the side wall of the pillars, enhanced size and contrast of the green region is expected for increasing fluence, as demonstrated by Fig. 5(c) and (d).

By comparison with the literature, it is well-known that the structural and morphological properties of substrates may affect cell growth and aggregation [102–104]. Indeed, surface topography is one of the key parameters that have been focused on to investigate ECs responses, studying for example patterned silk fibroin films [104]. In particular, Ye and co-workers have shown that HUVECs are extremely sensitive to curvature, becoming elongated and aligned when grown on glass rods (10–400 μm diameters) [105]. The outcome of their work suggests that

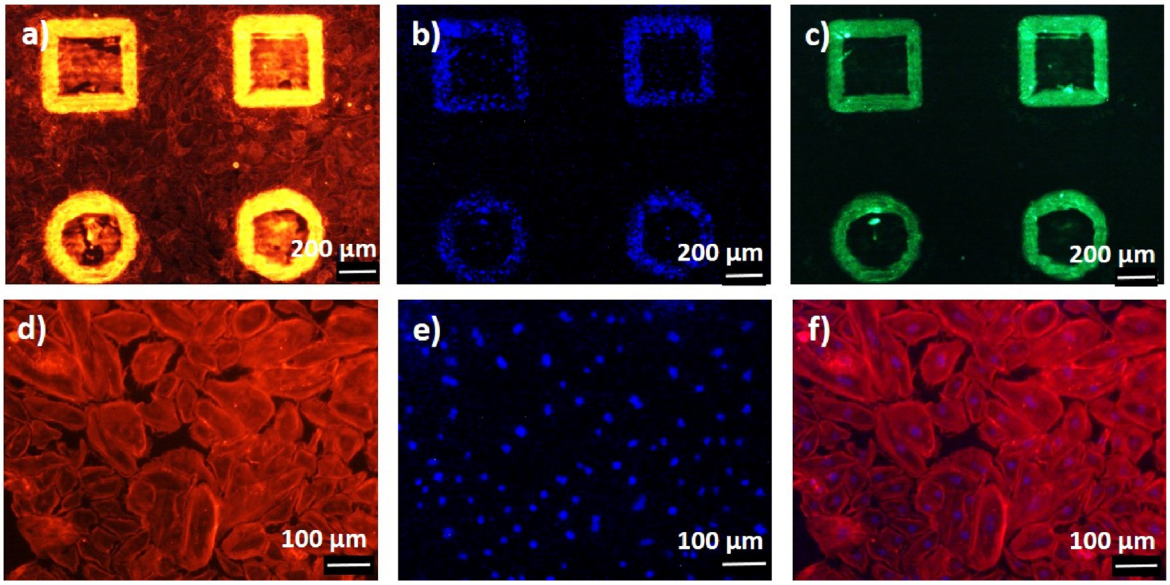

Fig. 4. Seeding of HUVECs on a) b) c) COC micro-pillars obtained by molding from ablated quartz micro-holes produced by treatment at P_{avg} = 40 W, c = 15, N_{steps} = 10 and on d) e) f) on flat COC substrate. The three channels represent the response of a) d) phallodin-TRITC (red), b) e) DAPI (blue), c) ZO-1 (green) and f) merge between phallodin-TRITC and DAPI. (For interpretation of the references to colour in this figure legend, the reader is referred to the Web version of this article.)

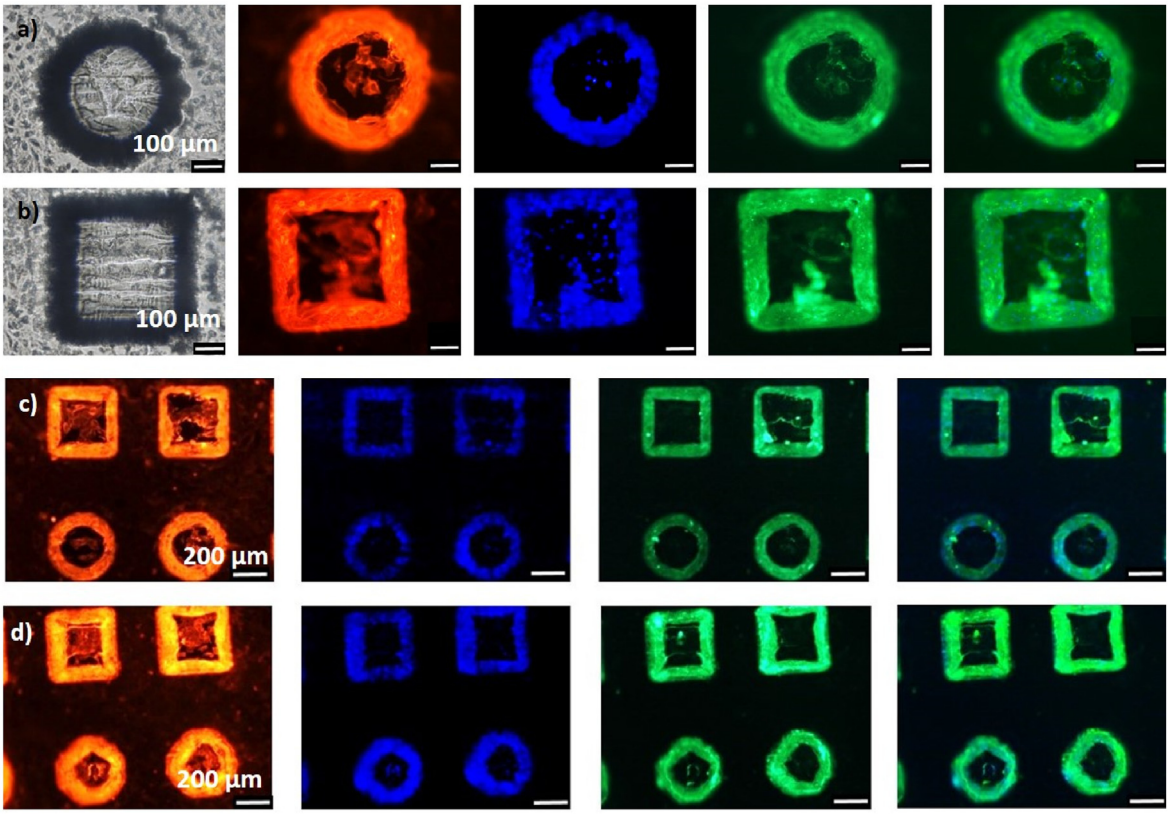

Fig. 5. Seeding of HUVECs on COC structures obtained by molding from ablated quartz micro-holes produced by treatment at c = 10, N_{steps} = 10 and (a)–(c) P_{avg} = 35 W and (d) P_{avg} = 40 W. (a), (b) The five channels represent the bright field, the response of phallodin-TRITC (red), DAPI (blue), ZO-1 (green) and merge between DAPI and ZO-1 channels. (c), (d) The four channels represent the response of phallodin-TRITC (red), DAPI (blue), ZO-1 (green) and merge between DAPI and ZO-1 channels. (For interpretation of the references to colour in this figure legend, the reader is referred to the Web version of this article.)

curvature has a similar effect to shear stress in vivo. Here, both square pyramidal and cylindrical pillars are wrapped with HUVECs having ZO-1 well expressed, suggesting that different 3D vertical structures presented in this study allow to obtain a tight endothelium.

Changes in expression of TJs proteins were associated to a different paracellular permeability in endothelial monolayer [106]. Indeed, under physiological conditions, TJs are strongly developed in ECs of the blood-brain barrier in order to strictly select the brain entry, but only moderately formed between ECs of the peripheral vasculature to allow many molecules to cross through the tissue [106]. Furthermore, TJs expression was shown to be negatively affected by the presence of pro-inflammatory cytokines, increasing the endothelial permeability in some pathological conditions [106]. Although we are conscious that further morphological and functional studies are needed to assess the 3D arrangement of HUVECs along the entire surface of the vertical walls of the micro-pillars, we envision the possibility of using micro-pillars arrays coated with HUVECs as a model to study endothelial permeability in the presence of inflammatory diseases or to select new anti-inflammatory drugs able to repair the damaged endothelial function. In this perspective, micro-pillars with characteristic length scales of hundreds of microns rather than a few microns are suitable substrates to study cellular organization and interactions without influencing the single cell arrangement. Indeed, in general micro-pillars with diameters ranging from a few to tens of microns are expected to deform and perturb the cell morphology because their size is close to the cell size. Furthermore, deformation of single cell morphology may alter natural cell-cell interactions as well as their functionality. For instance, HUVECs seeded on PDMS micro-pillars were found to arrange differently depending on diameter and spacing between micro-pillars [107]. Since endothelium cells are elongated and align in the direction of the blood flow, biomaterial surfaces enabling adhesion and elongated morphology are favourable conditions to study ECs function for biomedical applications requiring a support for the formation of an endothelial cell monolayer.

Our results indicate that the assembly and spreading of the HUVECs along the lateral walls of the micro-pillars are not affected from the pillar shape (square pyramidal and conical), meaning that edges don't perturb the cell-cell interaction distance for large enough pillar size. Noteworthy, beyond the final application, the role of the vertical wall roughness and texturing of the pillars on the assembly of the HUVECs is very intriguing, by comparison with pillars of similar size produced by traditional optical lithography. Indeed, optical lithography allows the realization of polymeric or inorganic pillars of rectangular and cylindrical shape with nanometer-scale roughness [108,109] that may influence the 3D self-assembly of HUVECs and the expression of the ZO-1 protein, indicating the presence of TJs. The presence of micro- and nano-textured surface topography is known to promote both adhesion and proliferation of HUVECs [110]. On the other hand, effective cellular adhesion was observed on un-patterned micron-rough substrates as well as grooved and wrinkled substrates [111,112]. Since laser surface texturing is an effective approach for micro-patterning of the surface of different materials, it is gaining huge potential in biomedical applications requiring micron-rough substrate for cell adhesion [113]. In the case of our experiments, the lateral surface of the COC micro-pillars exhibit ripple-like vertical features (Fig. 3) stemming from the CO_2-laser pathways that, consistently with the above reported literature, are expected to favor cell adhesion and alignment along their length.

4. Conclusion

A commercial CO_2-laser engraver was adapted to ablate micro-channels and micro-holes on quartz substrates. After optimization of the main parameters, CO_2-laser processing was demonstrated to be a fast,

flexible and maskless fabrication method to produce microfluidic reactors and micro-pillars for 3D cell culturing. Compared to standard methods for deep (≥100 μm) quartz etching mainly based on photolithography and wet etching, an unprecedented fast engraving (estimated rate of 34 μm/s) was obtained with a simpler and less expensive equipment in an un-controlled environment (no "clean room" needed), a reduced amount of chemicals, metals and polymers. For the production of micro-reactors, a post-ablation treatment in BOE solution was optimized to remove rims/ripples stemming from laser-texturing that compromise the perfect sealing to flat substrates. The assembled quartz/PDMS serpentine micro-reactors resulted very stable at the overall volumetric flow rate ranges usually applied to perform chemical reactions, that is from tens of μL/min up to 1 mL/min. The method can be easily extended to the production of pure quartz micro-reactors by fusion bonding of the CO_2-laser ablated quartz substrates to flat quartz surfaces to provide high chemicals, optically transparent, temperature and pressure resistant micro-reactors, with a wide range of applications.

We demonstrate not only the versatility of the fabrication approach in microfluidics but also its interesting potentialities and perspectives in the biological and medicine fields. Indeed, on the other hand, as-ablated micro-holes of conical and square pyramidal shapes were used as molds to fabricate COC micro-pillars that have been studied as 3D cell culture templates. By comparison with observation of cells' behavior on flat COC substrates, the shape and the roughness of the micro-pillars were found to drive a 3D compact organization of the HUVECs that expressed the ZO-1 proteins, indicating the formation of a tight epithelium. Beyond interesting studies regarding the influence of micro-structures roughness, shape and composition on cell assembly, these results suggest additional applications that can be subject of a further investigation. Considering the versatility of the approach, the quartz mold could be used to model hydrogel-based scaffolds and/or the laser ablation technique could be used to directly machine micro-pillars of biocompatible materials. When surrounded by HUVECs, micro-vessels with a hydrogel lumen may be realized and used as platform to test the permeability of the vessels to novel drugs or to study the metabolism of biomolecules regulating some physiological or pathological pathways.

Sample credit author statement

Elisabetta Perrone, Vita Guarino: Visualization, Investigation, Reviewing and Editing. Alessandra Zizzari, Monica Bianco, Lillo Raia, Francesco Ferrara: Conceptualization, Methodology, Data curation, Reviewing and Editing. Massimo Cuscunà: Data curation; Reviewing and Editing. Marco Mazzeo, Giuseppe Gigli, Lorenzo Moroni: Reviewing and Editing. Maura Cesaria, Valentina Arima: Conceptualization, Methodology, Writing, Reviewing and Editing, Supervision.

Declaration of competing interest

The authors declare that they have no known competing financial interests or personal relationships that could have appeared to influence the work reported in this paper.

Acknowledgements

The authors acknowledge the project "TECNOMED"- Tecnopolo per la medicina di Precisione Nanotec Lecce - Regione Puglia (CUP B84I18000540002) and the project "Cluster in Bioimaging" (cod. QZYCUM0, "Aiuti a sostegno dei cluster tecnologici regionali 2014", Bando Regione Puglia n. 399 del 28/07/2014) for the financial support.

Appendix A. Supplementary data

Supplementary data to this article can be found online at https://doi.org/10.1016/j.mtbio.2021.100163.

References

[1] G. Petrucci, D. Caputo, N. Lovecchio, F. Costantini, I. Legnini, I. Bozzoni, A. Nascetti, G. de Cesare, Multifunctional system-on-glass for lab-on-chip applications, Biosens. Bioelectron. 93 (2017) 315–321.
[2] H. Hirama, T. Satoh, S. Sugiura, K. Shin, R. Onuki-Nagasaki, T. Kanamori, T. Inoue, Glass-based organ-on-a-chip device for restricting small molecular absorption, J. Biosci. Bioeng. 127 (2019) 641–646.
[3] A. Zizzari, M. Cesaria, M. Bianco, L.L. del Mercato, M. Carraro, M. Bonchio, R. Rella, V. Arima, Mixing enhancement induced by viscoelastic micromotors in microfluidic platforms, Chem. Eng. J. 391 (2020) 123572.
[4] X. Mao, J.R. Waldeisen, B.K. Juluri, T.J. Huang, Hydrodynamically tunable optofluidic cylindrical microlens, Lab Chip 7 (2007) 1303–1308.
[5] A. Zizzari, V. Arima, A. Zacheo, G. Pascali, P.A. Salvadori, E. Perrone, D. Mangiullo, R. Rinaldi, Fabrication of SU-8 microreactors for radiopharmaceutical production, Microelectron. Eng. 88 (2011) 1664–1667.
[6] A. Zizzari, M. Bianco, E. Perrone, M.G. Manera, S. Cellamare, S. Ferorelli, R. Purgatorio, A. Scilimati, A. Tolomeo, V. Dimiccoli, R. Rella, V. Arima, Microfluidic pervaporation of ethanol from radiopharmaceutical formulations, Chemical Engineering and Processing - Process Intensification 141 (2019) 107539.
[7] V. Arima, G. Pascali, O. Lade, H.R. Kretschmer, I. Bernsdorf, V. Hammond, P. Watts, F. De Leonardis, M.D. Tarn, N. Pamme, B.Z. Cvetkovic, P.S. Dittrich, N. Vasovic, R. Duane, A. Jaksic, A. Zacheo, A. Zizzari, L. Marra, E. Perrone, P.A. Salvadori, R. Rinaldi, Radiochemistry on chip: towards dose-on-demand synthesis of PET radiopharmaceuticals, Lab Chip 13 (2013) 2328–2336.
[8] A. Zacheo, V. Arima, G. Pascali, P.A. Salvadori, A. Zizzari, E. Perrone, L. De Marco, G. Gigli, R. Rinaldi, Radioactivity resistance evaluation of polymeric materials for application in radiopharmaceutical production at microscale, Microfluid. Nanofluidics 11 (2011) 35–44.
[9] M. Bu, T. Melvin, G.J. Ensell, J.S. Wilkinson, A.G.R. Evans, A new masking technology for deep glass etching and its microfluidic application, Sensors and Actuators A: Physica 115 (2004) 476–482.
[10] C. Iliescu, B. Chen, J. Miao, On the wet etching of Pyrex glass, Sensors and Actuators A: Physica 143 (2008) 154–161.
[11] A. Zacheo, A. Zizzari, E. Perrone, L. Carbone, G. Giancane, L. Valli, R. Rinaldi, V. Arima, Fast and safe microwave-assisted glass channel-shaped microstructure fabrication, Lab Chip 15 (2015) 2395–2399.
[12] X. Li, T. Abe, M. Esashi, Deep reactive ion etching of Pyrex glass using SF6 plasma, Sensors and Actuators A: Physica 87 (2001) 139–145.
[13] X. Li, T. Abe, Y. Liu, M. Esashi, Fabrication of high-density electrical feed-throughs by deep-reactive-ion etching of Pyrex glass, Journal of Microelectromechanical Systems 11 (2002) 625–630.
[14] C.-Y. Huang, C.-H. Kuo, W.-T. Hsiao, K.-C. Huang, S.-F. Tseng, C.-P. Chou, Glass biochip fabrication by laser micromachining and glass-molding process, J. Mater. Process. Technol. 212 (2012) 633–639.
[15] J. Ju, S. Lim, J. Seok, S.-m. Kim, A method to fabricate Low-Cost and large area vitreous carbon mold for glass molded microstructures,, Int. J. Precis. Eng. Manuf. 16 (2015) 287–291.
[16] T. Wang, J. Chen, T. Zhou, L. Song, Fabricating Microstructures on Glass for Microfluidic Chips by Glass Molding Process, Micromachines, Basel, 2018, 9.
[17] K.-H. Nguyen, P.A. Lee, B.H. Kim, Experimental investigation of ECDM for fabricating micro structures of quartz, Int. J. Precis. Eng. Manuf. 16 (2015) 5–12.
[18] X.D. Cao, B.H. Kim, C.N. Chu, Hybrid micromachining of glass using ECDM and micro grinding, Int. J. Precis. Eng. Manuf. 14 (2013) 5–10.
[19] N. Convery, N. Gadegaard, 30 years of microfluidics, Micro and Nano Engineering 2 (2019) 76–91.
[20] L.A. Hof, J. Abou Ziki, Micro-Hole Drilling on Glass Substrates—A Review, Micromachines, Basel, 2017, p. 53, 8.
[21] C.K. Malek, L. Robert, J.-J. Boy, P. Blind, Deep microstructuring in glass for microfluidic applications, Microsyst. Technol. 13 (2007) 447–453.
[22] N.H. Rizvi, P. Apte, Developments in laser micro-machining techniques, J. Mater. Process. Technol. 127 (2002) 206–210.
[23] A.B. Azouz, M. Vázquez, B. Paull, D. Brabazon, Laser processing of quartz for microfluidic device fabrication, Adv. Mater. Res. 445 (2012) 436–441.
[24] K.L. Wlodarczyk, D.P. Hand, M.M. Maroto-Valer, Maskless, rapid manufacturing of glass microfluidic devices using a picosecond pulsed laser, Sci. Rep. 9 (2019) 20215.
[25] D. Snakenborg, H. Klank, J.P. Kutter, Microstructure fabrication with a CO2 laser system, J. Micromech. Microeng. 14 (2003) 182–189.
[26] I.H. Chowdhury, X. Xu, A.M. Weiner, Ultrafast double-pulse ablation of fused silica, Appl. Phys. Lett. 86 (2005) 151110.
[27] A. Butkute, L. Jonušauskas, 3D manufacturing of glass microstructures using femtosecond laser, Micromachines 12 (2021) 499.
[28] K.M. Nowak, H.J. Baker, D.R. Hall, Analytical model for CO2 laser ablation of fused quartz, Appl. Opt. 54 (2015) 8653–8663.
[29] K. Zimmer, A. Braun, R. Böhme, Etching of fused silica and glass with excimer laser at 351 nm, Applied Surface Science 208-209, 2003, pp. 199–204.
[30] K.L. Wlodarczyk, N.J. Weston, M. Ardron, D.P. Hand, Direct CO2 laser-based generation of holographic structures on the surface of glass, Opt Express 24 (2016) 1447–1462.
[31] K.L. Wlodarczyk, A. Brunton, P. Rumsby, D.P. Hand, Picosecond laser cutting and drilling of thin flex glass, Opt Laser. Eng. 78 (2016) 64–74.
[32] D. Nieto, J. Arines, G.M. O'Connor, M.T. Flores-Arias, Single-pulse laser ablation threshold of borosilicate, fused silica, sapphire, and soda-lime glass for pulse widths of 500 fs, 10 ps, 20 ns, Appl. Opt. 54 (2015) 8596–8601.

[33] C. Buerhop, B. Blumenthal, R. Weissmann, N. Lutz, S. Biermann, Glass surface treatment with excimer and CO2 lasers, Appl. Surf. Sci. 46 (1990) 430–434.
[34] J. Ihlemann, B. Wolff, P. Simon, Nanosecond and femtosecond excimer laser ablation of fused silica, Appl. Phys. A 54 (1992) 363–368.
[35] M.-H. Yen, J.-Y. Cheng, C.-W. Wei, Y.-C. Chuang, T.-H. Young, Rapid cell-patterning and microfluidic chip fabrication by crack-free CO2 laser ablation on glass, J. Micromech. Microeng. 16 (2006) 1143–1153.
[36] D. Moore, M. Rahman, D.P. Dowling, P.J. McNally, D. Brabazon, Laser machined macro and micro structures on glass for enhanced light trapping in solar cells, Appl. Phys. A 110 (2013) 661–665.
[37] T. Kim, K.-K. Kwon, C.N. Chu, K.Y. Song, Experimental investigation on CO2 laser-assisted micro-slot milling characteristics of borosilicate glass, Precis. Eng. 63 (2020) 137–147.
[38] X.R. Du, X.F. Song, Y.C. Sun, X.Q. Zhang, H. Wang, X.H. Yang, Deep wet etching uniformity of polished fused silica glass, Key Eng. Mater. 726 (2017) 404–408.
[39] A. Zizzari, M. Bianco, R. Miglietta, L.L. del Mercato, M. Carraro, A. Sorarù, M. Bonchio, G. Gigli, R. Rinaldi, I. Viola, V. Arima, Catalytic oxygen production mediated by smart capsules to modulate elastic turbulence under a laminar flow regime, Lab Chip 14 (2014) 4391–4397.
[40] M. Bianco, A. Zizzari, L. Gazzera, P. Metrangolo, G. Gigli, I. Viola, V. Arima, Integrated microfluidic viscometer for edible oil analysis, Sensors and Actuators B: Chemicals 265 (2018) 91–97.
[41] A. Cutarelli, S. Ghio, J. Zasso, A. Speccher, G. Scarduelli, M. Roccuzzo, M. Crivellari, N. Maria Pugno, S. Casarosa, M. Boscardin, L. Conti, Vertically-aligned functionalized silicon micropillars for 3D culture of human pluripotent stem cell-derived cortical progenitors, Cells 9 (2020) 88.
[42] E. Tomecka, K. Zukowski, E. Jastrzebska, M. Chudy, Z. Brzozka, Microsystem with micropillar array for three- (gel-embaded) and two-dimensional cardiac cell culture, Sensors and Actuators B: Chemicals 254 (2018) 973–983.
[43] A. Zacheo, A. Quarta, A. Zizzari, A.G. Monteduro, G. Maruccio, V. Arima, G. Gigli, One step preparation of quantum dot-embedded lipid nanovesicles by a microfluidic device, RSC Adv. 5 (2015) 98576–98582.
[44] J.M. Khosrofian, B.A. Garetz, Measurement of a Gaussian laser beam diameter through the direct inversion of knife-edge data, Appl. Opt. 22 (1983) 3406–3410.
[45] B.H. Chueh, D. Huh, C.R. Kyrtsos, T. Houssin, N. Futai, S. Takayama, Leakage-free bonding of porous membranes into layered microfluidic array systems, Anal. Chem. 79 (2007) 3504–3508.
[46] A. Zizzari, M. Bianco, L.L. del Mercato, A. Sorarù, M. Carraro, P. Pellegrino, E. Perrone, A.G. Monteduro, M. Bonchio, R. Rinaldi, I. Viola, V. Arima, Highly sensitive membrane-based pressure sensors (MePS) for real-time monitoring of catalytic reactions, Anal. Chem. 90 (2018) 7659–7665.
[47] L. Zhou, Y. Jiang, P. Zhang, H. Wei, W. Fan, X. Li, J. Zhu, Numerical and experimental investigation of morphological modification on fused silica using CO2 laser ablation, Materials 12 (2019) 4109.
[48] G. Allcock, P.E. Dyer, G. Elliner, H.V. Snelling, Experimental observations and analysis of CO2 laser-induced microcracking of glass, J. Appl. Phys. 78 (1995) 7295–7303.
[49] Bending Rayleigh, Of glass under long continued stress, Nature 145 (1940) 29, 29.
[50] M. Koide, R. Sato, T. Komatsu, K. Matusita, Apparent viscosity and relaxation mechanism of glasses below glass transition temperature, Phys. Chem. Glasses 38 (1997) 83–86.
[51] I. Steingoetter, H. Fouckhardt, Deep fused silica wet etching using an Au-free and stress-reduced sputter-deposited Cr hard mask, J. Micromech. Microeng. 15 (2005) 2130–2135.
[52] A. Grosse, M. Grewe, H. Fouckhardt, Deep wet etching of fused silica glass for hollow capillary optical leaky waveguides in microfluidic devices, J. Micromech. Microeng. 11 (2001) 257–262.
[53] T.-L. Chang, Z.-C. Chen, Y.-W. Lee, Y.-H. Li, C.-P. Wang, Ultrafast laser ablation of soda-lime glass for fabricating microfluidic pillar array channels, Microelectron. Eng. 158 (2016) 95–101.
[54] C. Weingarten, E. Uluz, A. Schmickler, K. Braun, E. Willenborg, A. Temmler, S. Heidrich, Glass processing with pulsed CO2 laser radiation, Appl. Opt. 56 (2017) 777–783.
[55] H. Ogura, Y. Yoshida, Hole drilling of glass substrates with a CO2Laser, Jpn. J. Appl. Phys. 42 (2003) 2881–2886.
[56] G.A.J. Markillie, H.J. Baker, F.J. Villarreal, D.R. Hall, Effect of vaporization and melt ejection on laser machining of silica glass micro-optical components, Appl. Opt. 41 (2002) 5660–5667.
[57] W.W. Duley, W.A. Young, Kinetic effects in drilling with the CO2 laser, J. Appl. Phys. 44 (1973) 4236–4237.
[58] S. Prakash, S. Kumar, Fabrication of microchannels on transparent PMMA using CO2 Laser (10.6 μm) for microfluidic applications: an experimental investigation, Int. J. Precis. Eng. Manuf. 16 (2015) 361–366.
[59] X.-W. Cao, Q.-D. Chen, H. Fan, L. Zhang, S. Juodkazis, H.-B. Sun, Liquid-Assisted femtosecond laser precision-machining of silica, Nanomaterials 8 (2018) 287.
[60] B.Z. Cvetković, O. Lade, L. Marra, V. Arima, R. Rinaldi, P.S. Dittrich, Nitrogen supported solvent evaporation using continuous-flow microfluidics, RSC Adv. 2 (2012) 11117–11122.
[61] J. Zhao, J. Sullivan, T.D. Bennett, Wet etching study of silica glass after CW CO2 laser treatment, Appl. Surf. Sci. 225 (2004) 250–255.
[62] G. Kopitkovas, V. Deckert, T. Lippert, F. Raimondi, C.W. Schneider, A. Wokaun, Chemical and structural changes of quartz surfaces due to structuring by laser-induced backside wet etching, Phys. Chem. Chem. Phys. 10 (2008) 3195–3202.
[63] L. Ceriotti, K. Weible, N.F. de Rooij, E. Verpoorte, Rectangular channels for lab-on-a-chip applications, Microelectronic Engineering 67-68, 2003, pp. 865–871.
[64] E. Yakhshi-Tafti, H.J. Cho, R. Kumar, Diffusive mixing through velocity profile variation in microchannels, Exp. Fluid 50 (2011) 535–545.
[65] A. Zizzari, L. Carbone, M. Cesaria, M. Bianco, E. Perrone, F. Rendina, V. Arima, Continuous flow scalable production of injectable size-monodisperse nanoliposomes in easy-fabrication milli-fluidic reactors, Chem. Eng. Sci. 235 (2021) 116481.
[66] A. Zizzari, M. Bianco, L. Carbone, E. Perrone, F. Amato, G. Maruccio, F. Rendina, V. Arima, Continuous-flow production of injectable liposomes via a microfluidic approach, Materials 10 (2017) 1411.
[67] L. Marra, V. Fusillo, C. Wiles, A. Zizzari, P. Watts, R. Rinaldi, V. Arima, Sol–gel catalysts as an efficient tool for the kumada-corriu reaction in continuous flow, Sci. Adv. Mater. 5 (2013) 475–483.
[68] M. Shimbo, K. Furukawa, K. Fukuda, K. Tanzawa, Silicon-to-silicon direct bonding method, J. Appl. Phys. 60 (1986) 2987–2989.
[69] J. Ng Lee, C. Park, G.M. Whitesides, Solvent compatibility of poly(dimethylsiloxane)-based microfluidic devices, Anal. Chem. 75 (2003) 6544–6554.
[70] M. Cesaria, V. Arima, S. Rella, C. Malitesta, M.C. Martucci, M.G. Manera, A. Tolomeo, A. Scilimati, R. Rella, [^{18}F]F-DOPA synthesis by poly(dimethylsiloxane)-based platforms: thermal aging protocol to reduce chemicals-induced damage, Sensor. Actuator. B Chem. 254 (2017) 143–152.
[71] A. Martin, S. Teychené, S. Camy, J. Aubin, Fast and inexpensive method for the fabrication of transparent pressure-resistant microfluidic chips, Microfluid. Nanofluidics 20 (2016) 92–99.
[72] A. Borók, K. Laboda, A. Bonyár, PDMS bonding technologies for microfluidic applications: a review, Chem. Eng. Sci. 189 (2018) 431–448.
[73] E. Sollier, C. Murray, P. Maoddi, D. Di Carlo, Rapid prototyping polymers for microfluidic devices and high pressure injections, Lab Chip 11 (2011) 3752–3765.
[74] M. Kim, B.-U. Moon, C.H. Hidrovo, Enhancement of the thermo-mechanical properties of PDMS molds for the hot embossing of PMMA microfluidic devices, J. Micromech. Microeng. 23 (2013) 95024.
[75] G. Camino, S.M. Lomakin, M. Lazzari, Polydimethylsiloxane thermal degradation Part 1. Kinetic aspects, Polymer 42 (2001) 2395–2402.
[76] I. Kourmpetis, A.S. Kastania, K. Ellinas, K. Tsougeni, M. Baca, W. De Malsche, E. Gogolides, Gradient-temperature hot-embossing for dense micropillar array fabrication on thick cyclo-olefin polymeric plates: an example of a microfluidic chromatography column fabrication, Micro and Nano Engineering 5 (2019) 100042.
[77] L. Sainiemi, T. Nissilä, R. Kostiainen, S. Franssila, R.A. Ketola, A microfabricated micropillar liquid chromatographic chip monolithically integrated with an electrospray ionization tip,, Lab Chip 12 (2012) 325–332.
[78] B. Su, Y. Wu, Y. Tang, Y. Chen, W. Cheng, L. Jiang, Free-standing 1D assemblies of plasmonic nanoparticles, Adv. Mater. 25 (2013) 3968–3972.
[79] Z. Lao, Y. Zheng, Y. Dai, Y. Hu, J. Ni, S. Ji, Z. Cai, Z.J. Smith, J. Li, L. Zhang, D. Wu, J. Chu, Nanogap plasmonic structures fabricated by switchable capillary-force driven self-assembly for localized sensing of anticancer medicines with microfluidic SERS, Adv. Funct. Mater. 30 (2020) 1909467.
[80] C. Chen, V. Rengarajan, A. Kjar, Y. Huang, A matrigel-free method to generate matured human cerebral organoids using 3D-Printed microwell arrays,, Bioactive Materials 6 (2021) 1130–1139.
[81] C.-K. Huang, G.J. Paylaga, S. Bupphathong, K.-H. Lin, Spherical microwell arrays for studying single cells and microtissues in 3D confinement, Biofabrication 12 (2020) 25016.
[82] C. Hahn, M.A. Schwartz, Mechanotransduction in vascular physiology and atherogenesis, Nat. Rev. Mol. Cell Biol. 10 (2009) 53–62.
[83] C.F. Natale, J. Lafaurie-Janvore, M. Ventre, A. Babataheri, A.I. Barakat, Focal adhesion clustering drives endothelial cell morphology on patterned surfaces, J. R. Soc. Interface 16 (2019) 20190263.
[84] G. Tullii, F. Giona, F. Lodola, S. Bonfadini, C. Bossio, S. Varo, A. Desii, L. Criante, C. Sala, M. Pasini, C. Verpelli, F. Galeotti, M.R. Antognazza, High-aspect-ratio semiconducting polymer pillars for 3D cell cultures, ACS Appl. Mater. Interfaces 11 (2019) 28125–28137.
[85] F. Viela, D. Granados, A. Ayuso-Sacido, I. Rodríguez, Biomechanical cell regulation by high aspect ratio nanoimprinted pillars, Adv. Funct. Mater. 26 (2016) 5599–5609.
[86] S. Bonde, N. Buch-Månson, K.R. Rostgaard, T.K. Andersen, T. Berthing, K.L. Martinez, Exploring arrays of vertical one-dimensional nanostructures for cellular investigations, Nanotechnology 25 (2014) 362001.
[87] A.M. Greiner, A. Sales, H. Chen, S.A. Biela, D. Kaufmann, R. Kemkemer, Nano- and microstructured materials for in vitro studies of the physiology of vascular cells, Beilstein J. Nanotechnol. 7 (2016) 1620–1641.
[88] J. Paek, J. Kim, Microsphere-assisted fabrication of high aspect-ratio elastomeric micropillars and waveguides, Nat. Commun. 5 (2014) 3324.
[89] M.W. Toepke, D.J. Beebe, PDMS absorption of small molecules and consequences in microfluidic applications, Lab Chip 6 (2006) 1484–1486.
[90] V. Arima, M. Bianco, A. Zacheo, A. Zizzari, E. Perrone, L. Marra, R. Rinaldi, Fluoropolymers coatings on polydimethylsiloxane for retarding swelling in toluene, Thin Solid Films 520 (2012) 2293–2300.
[91] P.S. Nunes, P.D. Ohlsson, O. Ordeig, J.P. Kutter, Cyclic olefin polymers: emerging materials for lab-on-a-chip applications, Microfluid. Nanofluidics 9 (2010) 145–161.
[92] A. Bhattacharyya, C.M. Klapperich, Thermoplastic microfluidic device for on-chip purification of nucleic acids for disposable diagnostics, Anal. Chem. 78 (2006) 788–792.

[93] S.H. Choi, D.S. Kim, T.H. Kwon, Microinjection molded disposable microfluidic lab-on-a-chip for efficient detection of agglutination, Microsyst. Technol. 15 (2009) 309–316.
[94] D. Franco, M. Klingauf, M. Bednarzik, M. Cecchini, V. Kurtcuoglu, J. Gobrecht, D. Poulikakos, A. Ferrari, Control of initial endothelial spreading by topographic activation of focal adhesion kinase, Soft Matter 7 (2011) 7313–7324.
[95] M. Hansen, D. Nilsson, D. Johansen, S. Balslev, A. Kristensen, A nanoimprinted polymer lab-on-a-chip with integrated optics (SPIE, 2005.
[96] B. Bilenberg, L.H. Frandsen, T. Nielsen, M. Vogler, P.I. Borel, A. Kristensen, in: Conference on Lasers and Electro-Optics/Quantum Electronics and Laser Science Conference and Photonic Applications Systems Technologies, (Optical Society of America, Long Beach, California, 2006.
[97] J. Kameoka, R. Orth, B. Ilic, D. Czaplewski, T. Wachs, H.G. Craighead, An electrospray ionization source for integration with microfluidics, Anal. Chem. 74 (2002) 5897–5901.
[98] J. Steigert, S. Haeberle, T. Brenner, C. Müller, C.P. Steinert, P. Koltay, N. Gottschlich, H. Reinecke, J. Rühe, R. Zengerle, J. Ducrée, Rapid prototyping of microfluidic chips in COC, J. Micromech. Microeng. 17 (2007) 333–341.
[99] M. Virumbrales-Muñoz, J.M. Ayuso, M.M. Gong, M. Humayun, M.K. Livingston, K.M. Lugo-Cintrón, P. McMinn, Y.R. Álvarez-García, D.J. Beebe, Microfluidic lumen-based systems for advancing tubular organ modeling, Chem. Soc. Rev. 49 (2020) 6402–6442.
[100] H.W. Wang, C.W. Cheng, C.W. Li, H.W. Chang, P.H. Wu, G.J. Wang, Fabrication of pillared PLGA microvessel scaffold using femtosecond laser ablation, Int. J. Nanomed. 7 (2012) 1865–1873.
[101] J.D. Zawislak, K.W. Kolasinski, B.P. Helmke, Development of endothelial cells on pillar-covered silicon, physica status solidi (a) 206 (2009) 1356–1360.
[102] M. Bianco, A. Zizzari, P. Priore, L. Moroni, P. Metrangolo, M. Frigione, R. Rella, A. Gaballo, V. Arima, Lab-on-a-brane for spheroid formation, Biofabrication 11 (2019) 21002.
[103] Y. Yang, K. Wang, X. Gu, K.W. Leong, Biophysical regulation of cell behavior—cross talk between substrate stiffness and nanotopography, Engineering 3 (2017) 36–54.
[104] X. Du, Y. Wang, L. Yuan, Y. Weng, G. Chen, Z. Hu, Guiding the behaviors of human umbilical vein endothelial cells with patterned silk fibroin films, Colloids and Surfaces B: Biointerfaces 122 (2014) 79–84.
[105] M. Ye, H.M. Sanchez, M. Hultz, Z. Yang, M. Bogorad, A.D. Wong, P.C. Searson, Brain microvascular endothelial cells resist elongation due to curvature and shear stress, Sci. Rep. 4 (2014) 4681.
[106] C. Förster, Tight junctions and the modulation of barrier function in disease, Histochem. Cell Biol. 130 (2008) 55–70.
[107] Y. An, C. Ma, C. Tian, L. Zhao, L. Pang, Q. Tu, J. Xu, J. Wang, On-chip assay of the effect of topographical microenvironment on cell growth and cell-cell interactions during wound healing, Biomicrofluidics 9 (2015) 64112.
[108] L. Sun, W. Yang, H. Chu, R. Yang, H. Yu, Dynamic fabrication of microfluidic systems for particles separation based on optical projection lithography, Biomed. Microdevices 22 (2020) 80.
[109] M.S. Chiriacò, M. Bianco, F. Amato, E. Primiceri, F. Ferrara, V. Arima, G. Maruccio, Fabrication of interconnected multilevel channels in a monolithic SU-8 structure using a LOR sacrificial layer, Microelectron. Eng. 164 (2016) 30–35.
[110] T.W. Chung, D.Z. Liu, S.Y. Wang, S.S. Wang, Enhancement of the growth of human endothelial cells by surface roughness at nanometer scale, Biomaterials 24 (2003) 4655–4661.
[111] A. Ranjan, T.J. Webster, Increased endothelial cell adhesion and elongation on micron-patterned nano-rough poly(dimethylsiloxane) films, Nanotechnology 20 (2009) 305102.
[112] Y. Liu, W. Deng, L. Yang, X. Fu, Z. Wang, P. van Rijn, Q. Zhou, T. Yu, Biointerface topography mediates the interplay between endothelial cells and monocytes, RSC Adv. 10 (2020) 13848–13854.
[113] I. Shivakoti, G. Kibria, R. Cep, B.B. Pradhan, A. Sharma, Laser surface texturing for biomedical applications: a review,, Coatings 11 (2021) 124.